Int. J. Heat Mass Transfer. Vol. 31, No. 10, pp. 2147–2160, 1988
Printed in Great Britain

0017-9310/88 $3.00+0.00

Numerical simulation of binary solidification in a vertical channel with thermal and solutal mixed convection

W. D. BENNON
Aluminum Company of America, Alcoa Center, PA 15069, U.S.A.

and

F. P. INCROPERA
Heat Transfer Laboratory, School of Mechanical Engineering, Purdue University, West Lafayette, IN 47907, U.S.A.

(*Received* 20 *January* 1988 *and in final form* 31 *March* 1988)

Abstract—A continuum model is used to investigate the solidification of an aqueous ammonium chloride solution in the presence of an imposed forced flow. Calculations are performed to determine the effect of flow rate, chill wall temperature, and entry liquid composition on momentum, energy and species transfer within both the multiphase and bulk liquid regions. Small mass flow rates and small solidification rates are shown to enhance the free flow of chilled and water-enriched interdendritic fluids across the permeable liquidus front and hence to enhance species redistribution.

1. INTRODUCTION

Due to its significance in many industrial and scientific processes such as casting, welding, and crystal growth, multiconstituent, solid–liquid phase change has received considerable attention during the last two decades. However, with coexistence of solid and liquid phases in a multiphase (*mushy*) region, multiconstituent phase change processes are much more complex than those involving a pure substance. Unlike the description of transport behavior in the pure solid and liquid regions, macroscopic equations of transport are not well established in the multiphase region. Mathematical descriptions necessarily incorporate numerous microscopic and atomic level approximations which are specific to the phase change material, as well as the phase change environment.

Investigations of binary phase change in closed systems of varying geometry have been reported [1–6]. These studies confirm the influence of mushy region flows on energy transport and the history dependent macroscopic redistribution of species which occurs during solidification. In addition, transport in the multiphase region is shown to be coupled to naturally induced fluid motion in the adjoining bulk fluid, with the extent of this coupling depending on the relative strengths of solutally driven mushy region flows and thermally driven flows in the bulk liquid (the *melt*) [5]. The advection of species enriched liquids within the multiphase region and across the permeable liquidus front leads to an undesirable macroscopic redistribution of constituents known as macrosegregation [6].

In many applications, fluid motion within a solidifying body is also induced, intentionally or otherwise, by external means. For example, charging of molten liquids into a casting induces bulk fluid motion which influences overall transport behavior [7]. In recognition of the significant influence of bulk and mushy region advection on solidification, techniques have been developed which permit the alteration of naturally induced flows. These techniques include the rotation of crystals in the Czochralski process, the introduction of externally imposed Coriolis fields [8], and electromagnetic stirring [9].

The analysis of solidification in open systems with externally imposed forced flows has focused exclusively on discrete phase change materials [10], with no consideration given to non-discrete multiconstituent systems. Applications involving multiconstituent solidification with internal forced flows include the freezing of heat exchanger working fluids in supply lines and solidification within the nozzles of industrial metal casting operations. Fundamentally, an analysis of multiconstituent phase change with forced flow in an open system would permit delineation of the coupled influence of forced and buoyancy driven flows in the mushy and melt regions on the phase change process.

In this study, solidification of a binary aqueous ammonium chloride solution is considered for downward, laminar mixed convection between vertical parallel plates symmetrically cooled below the eutectic temperature. Special consideration is given to the effects of the externally imposed flow, solidification contraction, and the competing influences of thermal and solutal buoyancy.

NOMENCLATURE

c	specific heat
D	mass diffusion coefficient
D_h	hydraulic diameter, $2W$
f	mass fraction
f^*	dimensionless mass fraction
$\bar{f}$	total mass fraction, (solid mass)/(total mass)
Fo_s	solid phase Fourier number, $\alpha_s t/D_h^2$
g	volume fraction or gravitational acceleration
h	enthalpy
h^*	dimensionless enthalpy, $(h-h_{sol})/(h_{liq}-h_{sol})$
h_f	heat of fusion
k	thermal conductivity
k_p	equilibrium partition ratio, m_{liq}/m_{sol}
K	permeability
K_0	permeability coefficient
L	chill region length
L_{en}	adiabatic entry length
L_{ex}	adiabatic exit length
m	slope
p	pressure or isotropic stress component
$\bar{q}$	average wall heat flux
$\bar{q}^*$	average dimensionless heat flux, $\bar{q}D_h/k_l(T_0-T_e)$
Re	Reynolds number, U_0D_h/ν_l
Ste_s	solid phase Stefan number, $c_s(T_0-T_e)/h_f$
t	time
t^*	dimensionless time, $Fo_s\,Ste_s$
T	temperature
T^*	dimensionless temperature
T_m	fusion temperature for $f_l^\alpha = 0$
u, v	velocity components in the x- and y-directions
u^*, v^*	dimensionless velocity components, $u/U_0, v/U_0$
U_0	entry velocity
$\mathbf{V}$	velocity vector
W	plate spacing
x, y	Cartesian coordinates.

Greek symbols

α	thermal diffusivity, $k/\rho c$
β_S	solutal expansion coefficient
β_T	thermal expansion coefficient
μ	dynamic viscosity
ν	kinematic viscosity
ρ	density
ψ	stream function.

Subscripts

c	cold boundary
e	eutectic
k	phase k
l	liquid
liq	liquidus
m	evaluated at T_m
s	solid
sol	solidus
0	entry.

Superscript

α	constituent α (water).

2. MATHEMATICAL MODEL

Solidification is considered within a vertical, two-dimensional parallel plate channel as shown in Fig. 1. Initially, the entire channel ($-L_{en} \leqslant x \leqslant L+L_{ex}$) is insulated and superheated binary phase change material of temperature T_0 and composition $f_{l,0}^\alpha$ enters at $x = -L_{en}$. At time $t = 0$, both vertical boundaries ($0 \leqslant x \leqslant L$) are brought to, and maintained at, a temperature T_c which is below the eutectic temperature T_e.

Continuum equations governing the conservation of mass, momentum, energy and species have been previously developed [11] and, for the system of interest, may be expressed as

$$\frac{\partial}{\partial t}(\rho)+\nabla\cdot(\rho\mathbf{V}) = 0 \tag{1}$$

$$\frac{\partial}{\partial t}(\rho u)+\nabla\cdot(\rho\mathbf{V}u) = \nabla\cdot\left(\mu_l\frac{\rho}{\rho_l}\nabla u\right)-\frac{\mu_l}{K}\frac{\rho}{\rho_l}(u)-\frac{\partial p}{\partial x} - \rho_l g[\beta_T(T-T_c)+\beta_S(f_l^\alpha-f_{l,c}^\alpha)] \tag{2}$$

$$\frac{\partial}{\partial t}(\rho v)+\nabla\cdot(\rho\mathbf{V}v) = \nabla\cdot\left(\mu_l\frac{\rho}{\rho_l}\nabla v\right)-\frac{\mu_l}{K}\frac{\rho}{\rho_l}(v)-\frac{\partial p}{\partial y} \tag{3}$$

$$\frac{\partial}{\partial t}(\rho h)+\nabla\cdot(\rho\mathbf{V}h) = \nabla\cdot\left(\frac{k}{c_s}\nabla h\right) +\nabla\cdot\left[\frac{k}{c_s}\nabla(h_s-h)\right]-\nabla\cdot[\rho(h_l-h)\mathbf{V}] \tag{4}$$

$$\frac{\partial}{\partial t}(\rho f^\alpha)+\nabla\cdot(\rho\mathbf{V}f^\alpha) = \nabla\cdot(\rho D\nabla f^\alpha) +\nabla\cdot[\rho D\nabla(f_l^\alpha-f^\alpha)]-\nabla\cdot[\rho(f_l^\alpha-f^\alpha)\mathbf{V}]. \tag{5}$$

The continuum density, velocity, enthalpy and species mass fraction are defined as

$$\rho = g_s\rho_s+g_l\rho_l \tag{6}$$

$$\mathbf{V} = f_l\mathbf{V}_l \tag{7}$$

$$h = f_sh_s+f_lh_l \tag{8}$$

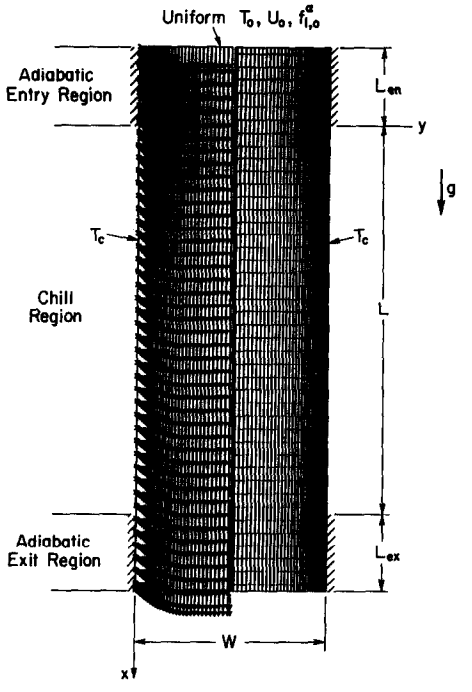

FIG. 1. Initial velocity field ($Re = 800$), nomenclature, and numerical grid relevant to binary solidification in a parallel plate channel.

$$f^{\alpha} = f_s f_s^{\alpha} + f_l f_l^{\alpha}. \tag{9}$$

Similarly, the continuum thermal conductivity and mass diffusion coefficient are

$$k = g_s k_s + g_l k_l \tag{10}$$

$$D = f_l D_l^{\alpha}. \tag{11}$$

In the buoyancy source terms, phase densities are assumed equal, and the Boussinesq approximation is invoked. The assumption of $\rho_s = \rho_l$ in the buoyancy terms is synonymous with the assumption of neutral phase buoyancy. Hence, floating or settling of dispersed phases is not considered in the present calculations. Phase thermophysical properties are assumed constant, and phase enthalpies are defined as

$$h_s = c_s T \tag{12}$$

$$h_l = c_l T + [(c_s - c_l) T_e + h_f] \tag{13}$$

where it is presumed that $h_s|_{T=0} = 0$ and that $(h_l - h_s)|_{T=T_e} = h_f$. Based on the availability of relevant geometric data [12], permeability is assumed to be isotropic and is related to the liquid volume fraction using the Kozeny–Carman (or Blake–Kozeny) equation

$$K = K_0 \left[\frac{g_l^3}{(1-g_l)^2} \right] \tag{14}$$

where K_0 is a constant which depends on the specific multiphase region morphology.

Closure of the system of conservation equations requires supplementary relationships for phase mass fractions and compositions. Assuming local compositional equilibrium and neglecting solidus and liquidus line curvature, the solid mass fraction and liquid phase composition can be expressed as [11]

$$f_s = \frac{1}{1-k_p} \left[\frac{T - T_{liq}}{T - T_m} \right] \tag{15}$$

$$f_l^{\alpha} = \frac{f^{\alpha}}{1 + f_s(k_p - 1)} \tag{16}$$

where T_{liq} is the liquidus temperature corresponding to f^{α}, T_m the fusion temperature as $f^{\alpha} \to 0$, and k_p the equilibrium partition ratio ($k_p = m_{liq}/m_{sol}$). Equations (15) and (16) are valid only in the multiphase region. Above the liquidus temperature, the solid mass fraction is identically zero ($f_s = 0$) and $f_l^{\alpha} = f^{\alpha}$. Similarly, below the solidus temperature, where $f_s = 1$, the liquid composition f_l^{α} has no physical significance.

Unlike the analysis of classical single phase, single constituent problems, difficulties arise when attempts are made to cast the transport equations into a meaningful dimensionless form [5]. Even if such a form could be developed, the large number of governing parameters would make it difficult to perform a comprehensive parametric investigation. Nevertheless, calculations performed using primitive variables may still be represented using dimensionless parameters which are based on length, velocity, temperature, and composition scales of D_h, U_0, $T_0 - T_e$, and $f_{l,e}^{\alpha} - f_{l,0}^{\alpha}$, respectively.

A widely accepted numerical finite-difference scheme [13] for the solution of coupled elliptic partial differential equations has been used to solve the governing continuum equations. Details regarding extension of this scheme to accommodate binary solid–liquid phase change, as well as the solution procedure itself, are provided in ref. [14]. The continuum model and solution procedures have been previously verified [5] through comparisons with both exact solutions and benchmark numerical solutions. In this study, calculations were performed for the symmetric half of a channel of fixed length and width ($L = 100$ mm, $W = 50$ mm) using the biased 34 node y-grid shown in Fig. 1. Previous grid studies [5] suggest that the present 34 node distribution suitably accommodates cross-stream variations in the dependent variables. Additional calculations were performed to investigate the effect of the x-grid dimensions. Predictions obtained for axial control volume dimensions of $\Delta x/L = 4.0 \times 10^{-2}$ and 3.3×10^{-2} yielded nearly indistinguishable results for global parameters such as the chill wall heat extraction ($\bar{q}_c$) and the total solid mass fraction ($\bar{f}_s$). Hence, a uniform x-grid characterized by $\Delta x/L = 3.3 \times 10^{-2}$ was used in all simulations.

The adiabatic entry (L_{en}) and exit (L_{ex}) lengths of the channel were selected to minimize their influences on predicted solidification behavior. For large entry mass flow rates ($Re = 800$), $L_{en}/L = L_{ex}/L = 0.2$ was found to be satisfactory. For small flow rates ($Re =$

Table 1. Thermophysical properties of NH_4Cl–H_2O

	Solid	Liquid
Specific heat (J kg^{-1} K^{-1})	1870	3249
Thermal conductivity (W m^{-1} K^{-1})	0.393	0.468
Density (kg m^{-3})	1102	1073
Diffusion coefficient (m^2 s^{-1})	—	4.8×10^{-9}
Viscosity (kg m^{-1} s^{-1})	—	1.3×10^{-3}
Latent heat of fusion, h_f (J kg^{-1})		3.138×10^5
Permeability coefficient, K_0 (m^2)		5.56×10^{-11}
Thermal expansion coefficient, β_T (K^{-1})		3.832×10^{-4}
Solutal expansion coefficient, β_S		0.257
Eutectic temperature, T_e (K)		257.75
Eutectic composition, $f_{l,e}^{H_2O}$		0.803
NH_4Cl melting point, T_m (K)		633.59
Equilibrium partition ratio, k_p		0.30

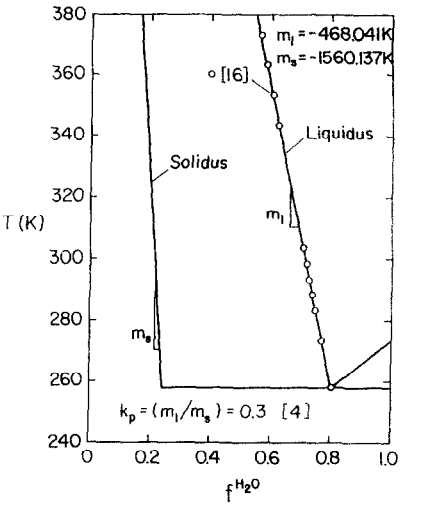

FIG. 2. Linearized NH_4Cl–H_2O phase diagram.

Table 2. Conditions of the calculations

Case	T_0 (K)	T_c (K)	$f_{1,0}^{H_2O}$	Re
1	298	233	0.72	200
2	298	233	0.72	800
3	298	243	0.72	200
4	298	233	0.73	800

200), however, the adiabatic regions were extended to $L_{en}/L = L_{ex}/L = 0.3$. Hence, calculations for $Re = 800$ and 200 were performed using 44×34 and 50×34 grids, respectively. For each Reynolds number, the corresponding single-phase hydrodynamic entry region problem was solved to obtain the initial channel velocity field. Comparisons made with previous investigations [15] revealed that, in terms of u_{max}/U_0, the initial velocity fields were accurate to within 10%. Maximum deviations, owing primarily to the sparse x-grid employed, occurred near the channel entrance. However, the rapid distortion of entry region velocity profiles due to downstream solidification suggests that these errors will have little effect on global phase change behavior.

A numerical time step of $\Delta t = 3$ s was used in all calculations. Iteration within a time step was employed and terminated when changes in the average heat extraction from the chilled wall $\bar{q}_c$, the total mass fraction solid $\bar{f}_s$, and the minimum and maximum compositions were each below 0.001%. Each numerical simulation was terminated when the solidification rate, $\partial\bar{f}_s/\partial t$, decreased to 6×10^{-5} s^{-1}.

Owing to its relatively well characterized thermophysical properties [5], calculations were performed for an aqueous ammonium chloride solution. These properties are summarized in Table 1, and the linearized phase diagram is shown in Fig. 2. To determine the relative effects of the externally imposed and buoyancy driven flows, calculations were performed for four sets of conditions corresponding to different inlet velocities (Reynolds numbers), wall temperatures, and inlet compositions (Table 2). Since the eutectic composition ($f_{l,e}^{H_2O} = 0.803$) exceeds the inlet composition, $f_{l,0}^{H_2O}$, water (the lighter component) is rejected due to solidification, creating a positive solutal buoyancy force in the mushy region.

3. RESULTS

Figures 3–6 illustrate velocity vector, streamline, isotherm, and liquid isocomposition distributions for Case 1 ($Re = 200$, $T_0 = 298$ K, $T_c = 233$ K, $f_{l,0}^{H_2O} = 0.72$) at selected times. Each plot corresponds to a one-half section of the channel which extends from one of the chilled walls to the symmetry midplane.

Since velocity vectors are based on the continuum components, velocities in the bulk fluid are actual velocities, while those in the multiphase region are superficial or discharge velocities. Solidus and liquidus contours included on the velocity plots represent lines corresponding to $h^* = 0$ and 1, respectively, where $h^* = (h-h_{sol})/(h_{liq}-h_{sol})$. Maximum stream functions associated with downflow in the liquid and clockwise rotation in the mushy and liquid regions near the channel entrance are designated as $\psi_{max,d}$ and $|\psi_{max,r}|$, respectively. In Figs. 3(b)–6(b) bulk liquid streamlines are plotted in increments of $\psi_{max,d}/10$, while streamlines associated with the clockwise rotating cells are plotted in increments of $|\psi_{max,r}|/6$. Isotherms depicted in Figs. 3(c)–6(c) represent lines of constant $T^* = (T-T_c)/(T_0-T_c)$, with the chilled boundary and channel entrance represented by $T^* = 0$ and 1, respectively. Liquid isocomposition lines shown in Figs. 3(d)–6(d) represent lines of constant $f_l^* = (f_l^{H_2O}-f_{l,0}^{H_2O})/(f_{l,e}^{H_2O}-f_{l,0}^{H_2O})$, with the channel entrance and solidus lines represented by $f_l^* = 0$ and 1, respectively. Both T^* and f_l^* are plotted in increments of 1/10.

Figure 3 illustrates conditions at $t^* = 5.51\times10^{-4}$ ($t = 120$ s). Solidification is initially characterized by rapid propagation of the liquidus into the bulk fluid. While the solidus and liquidus fronts remain nearly planar over a large portion of the chill section L,

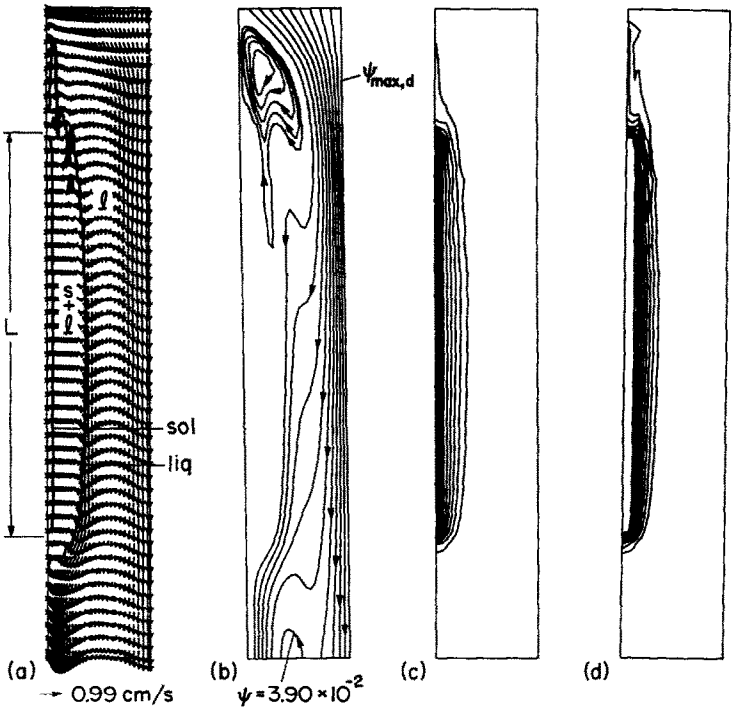

FIG. 3. Solidification behavior at $t = 120$ s ($t^* = 5.51 \times 10^{-4}$) for Case 1: (a) velocity vectors; (b) streamlines ($\psi_{max,d} = 6.5 \times 10^{-2}$, $|\psi_{max,r}| = 6.18 \times 10^{-3}$); (c) isotherms; (d) liquid isocomposition lines.

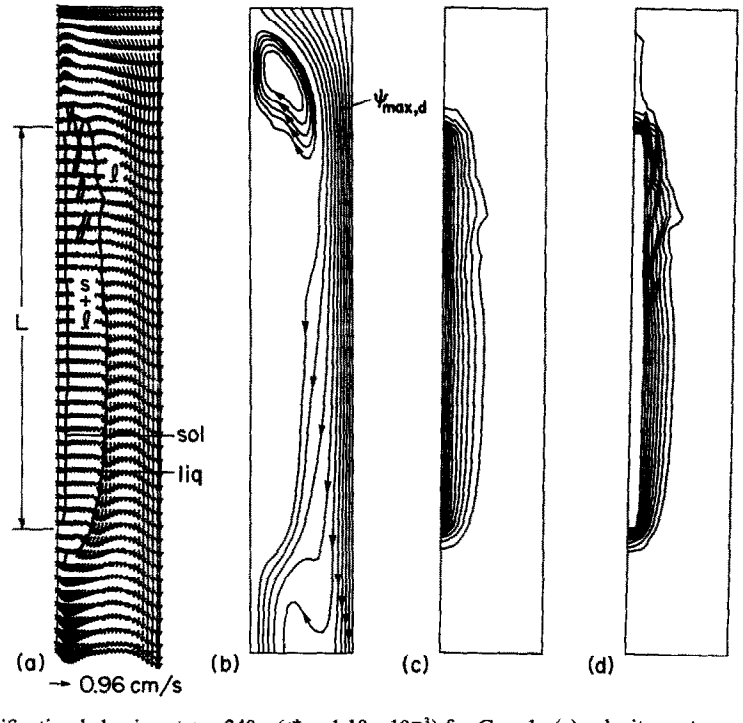

FIG. 4. Solidification behavior at $t = 240$ s ($t^* = 1.10 \times 10^{-3}$) for Case 1: (a) velocity vectors; (b) streamlines ($\psi_{max,d} = 6.50 \times 10^{-2}$, $|\psi_{max,r}| = 1.15 \times 10^{-2}$); (c) isotherms; (d) liquid isocomposition lines.

significant deviations from planarity occur near the entrance and exit regions. Due to axial diffusion, solidification is observed both upstream and downstream of the chill section. While the liquidus front downstream of the chill section remains smooth, irregularities develop near the chill section entrance ($x = 0$, Fig. 1). These irregularities are due primarily to the influence of advective species transport. For the small

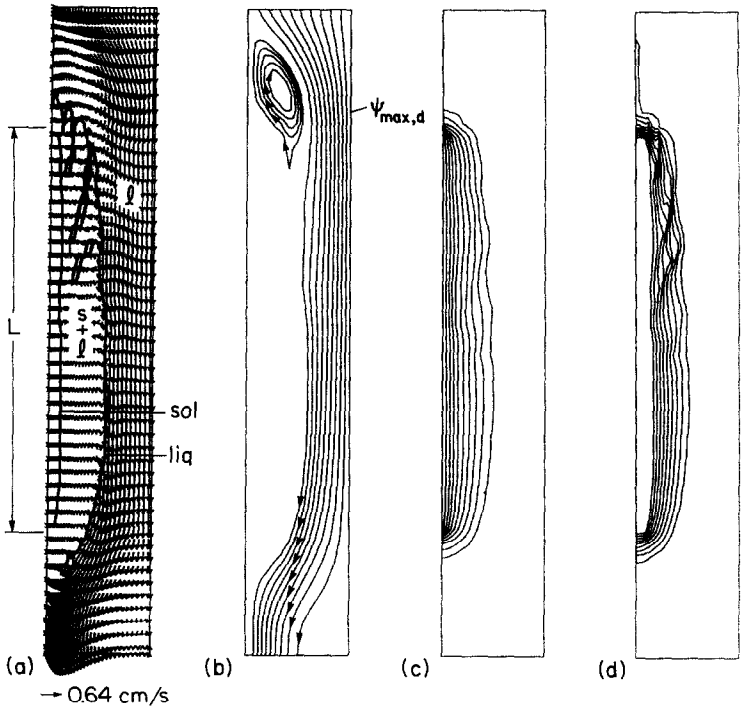

FIG. 5. Solidification behavior at $t = 480$ s ($t^* = 2.20 \times 10^{-3}$) for Case 1 : (a) velocity vectors ; (b) streamlines ($\psi_{max,d} = 6.50 \times 10^{-2}$, $|\psi_{max,r}| = 8.71 \times 10^{-3}$) ; (c) isotherms ; (d) liquid isocomposition lines.

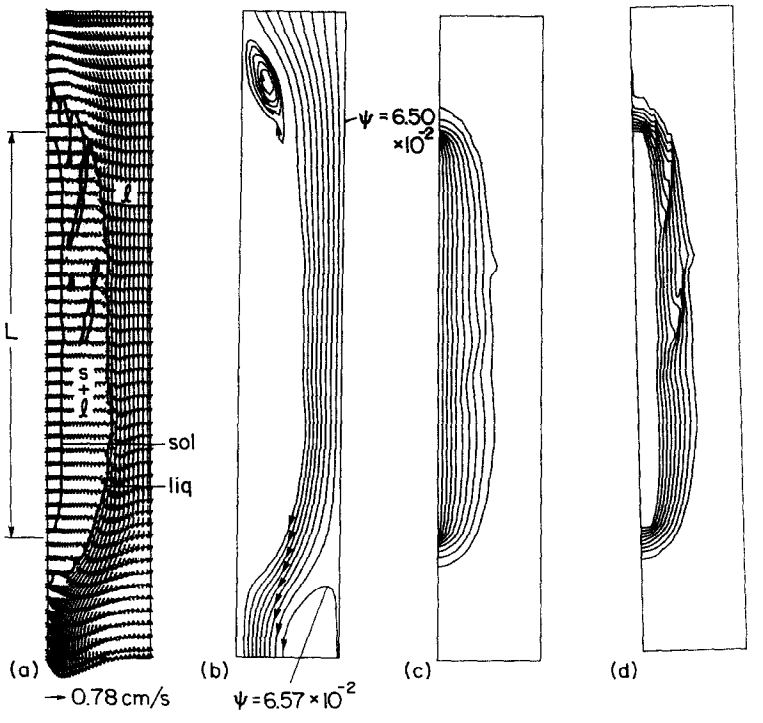

FIG. 6. Solidification behavior at $t = 960$ s ($t^* = 4.41 \times 10^{-3}$) for Case 1 : (a) velocity vectors ; (b) streamlines ($\psi_{max,d} = 7.30 \times 10^{-2}$, $|\psi_{max,r}| = 3.73 \times 10^{-3}$) ; (c) isotherms ; (d) liquid isocomposition lines.

Reynolds number of Case 1, solutally driven flows of lighter, water-rich interdendritic fluids are able to penetrate the liquidus front and ascend near the boundary of the adiabatic entrance region. However, this upflow is deflected downward by the externally imposed bulk fluid motion, and a clockwise recirculation cell is established (Fig. 3(b)). The outflow of chilled, water-rich, interdendritic fluids from the

mushy region near the chill section entrance is confirmed by the isotherm and liquid isocomposition lines shown in Figs. 3(c) and (d), respectively. It is the liquidus temperature depression which accompanies water enrichment of the liquid that is responsible for the observed liquidus front irregularities (Fig. 3(a)). Except for the entrance region and regions close to the liquidus front, the bulk liquid core remains nearly isothermal and free of significant composition gradients.

Flow conditions in the fluid core (Fig. 3(a)) are determined by constriction due to solidification, as well as by the competing influences of thermal and solutal buoyancy. While the aforementioned entrance region upflow is due to the dominance of solutal buoyancy forces, downflow in the fluid core adjacent to the liquidus front is due to the imposed forced flow and an assisting thermal buoyancy force. While bulk fluids near the channel midplane experience rapid longitudinal acceleration due to flow constriction, as indicated by the dense and nearly vertical streamlines of Fig. 3(b), fluid between the midplane and liquidus front decelerates as it is channeled toward the front to feed a strong thermally induced flow. Near the channel exit, the adverse pressure gradient established by the rapidly diverging flow is responsible for a rapid growth in the velocity boundary layer along the liquidus (Fig. 3(a)). While flow separation was not observed in the exit region, the inability of the imposed mass flow rate to feed the strong, thermally induced fluid acceleration resulted in the establishment of a weak inflow at the channel exit (Fig. 3(b)).

In all of the calculations of this study, the channel exit was assumed to be an outflow boundary [13], with axial diffusion neglected. The absence of significant temperature and concentration gradients at this boundary (Figs. 3(c) and (d)) justifies use of the outflow condition, despite the existence of a weak inflow. If significant temperature and/or composition gradients existed at the channel exit, such an assumption would become suspect and downstream transport behavior would have to be considered in more detail.

Solidification conditions at $t^* = 1.10 \times 10^{-3}$ ($t = 240$ s) are shown in Fig. 4. Persistence of the chilled and water-enriched interdendritic outflow strengthens the clockwise recirculation of bulk fluids in the adiabatic entry region (Fig. 4(b)). The strength of this cell ($|\psi_{\max,r}| = 1.5 \times 10^{-2}$) leads to the formation of a well-defined solutally driven boundary layer on the wall of the adiabatic entry region (Figs. 4(a) and (d)). While the entry length L_{en} was selected to minimize the influence of upstream conditions on solidification in the chill section for small Re, pronounced deflection of bulk fluid streamlines near the solutally driven recirculating cell suggests that downstream solidification may retain a modest dependence on L_{en}. Distortions in the liquidus front due to the water enrichment of bulk fluids persist near the chill section entrance. This water enrichment also leads to mushy region remelting upstream of the chill section. Small liquid pockets within the mushy region can also be observed (Fig. 4(a)) and are attributed to the liquidus temperature depression which accompanies water enrichment. While solutally driven flows exist within the mushy region, these flows are extremely weak relative to flows associated with the entry region recirculation and hence do not appear in the streamline plots of Fig. 4(b).

Isotherms shown in Fig. 4(c) suggest that the bulk fluid core remains free of significant temperature gradients. Distortions which appear near the liquidus front correspond to irregularities in the front morphology. With the exception of conditions near the wall of the adiabatic entry region, the bulk fluid remains free of significant composition gradients (Fig. 4(d)). Distortions in the isocomposition lines occur near the confined liquid pockets and the liquidus front irregularities.

Flow conditions in the bulk fluid core (Fig. 4(a)) are similar to those observed in Fig. 3(a). Fluid entering the channel accelerates rapidly due to the solidification induced flow constriction. Flow near the channel midplane remains nearly parallel to the chilled wall, while flow near the liquidus front decelerates as fluid is diverted to the front to feed the assisting, thermally induced flow. Significant boundary layer development on the liquidus near the exit region is again attributed to the adverse pressure gradients established by divergence of the flow cross-sectional area. While inflow at the channel exit is revealed by the velocity vectors of Fig. 4(a), it is extremely weak and confined to a very small region upstream of the channel exit.

Solidification behavior at $t^* = 2.20 \times 10^{-3}$ ($t = 480$ s) is shown in Fig. 5. While water-rich interdendritic outflow and the corresponding solutally driven recirculation persist in the entry region (Figs. 5(a) and (b)), the strength of the recirculation weakens ($|\psi_{\max,r}| = 8.71 \times 10^{-3}$), as the solidification rate declines. Previously observed liquid pockets within the mushy region have enlarged, forming channels oriented approximately 80° from the horizontal (Fig. 5(a)). Localized melting which accompanies water enrichment of these regions and the formation of discrete flow channels have been previously observed in qualitative experiments for static solidification [17, 18]. Similar behavior has also been identified by investigations dealing with freckling in unidirectional solidified castings [19]. The present results, however, represent the first prediction of such behavior for solidification in the presence of a forced flow.

As with earlier times, significant temperature and liquid concentration gradients are confined primarily to the solid and mushy regions (Figs. 5(c) and (d)). Irregularities in the liquid isocomposition lines within the mushy region (Fig. 5(d)) correspond to locations of the liquid channels.

Due to the significant reduction in cross-sectional area, flow conditions in the bulk fluid core (Figs. 5(a) and (b)) are dominated by forced convection. Here,

thermal boundary layer development observed on the liquidus front in the central region of the chill zone for previous times (Figs. 3(a) and 4(a)) is no longer evident and spanwise velocity distributions are nearly uniform. However, as fluid decelerates near the chill section exit, assisting thermal buoyancy adjacent to the chilled liquidus front again becomes significant relative to the forced flow. Hence, there is a resumption of boundary layer development near the chill section exit (Fig. 5(a)).

Figure 6 illustrates solidification behavior after 960 s ($t^* = 4.41 \times 10^{-3}$) and is representative of conditions approaching steady state ($\partial \bar{f}/\partial t = 6.4 \times 10^{-5}$ s^{-1}). Since the rejection of water-rich interdendritic fluids into the adiabatic entry region (Fig. 6(d)) has declined significantly, solutally driven boundary layer development on the wall of the entrance region (Fig. 6(a)) and the associated clockwise recirculation (Fig. 6(b)) are weak ($|\psi_{\max,r}| = 3.73 \times 10^{-3}$). Temperature and liquid composition gradients are again confined almost exclusively to the solid and mushy regions (Figs. 6(c) and (d)). Irregularities in liquid isocomposition lines are associated with liquid channels in the mushy region, and liquidus front irregularities established during the early stages of solidification persist in the chill section entrance (Fig. 6(a)). Moreover, the decline in the entrance region water concentration with time (Figs. 4(d)–6(d)) increases the local liquidus temperature, thereby enhancing upstream solidification (Figs. 4(a)–6(a)).

As observed in Fig. 5 for $t = 480$ s, conditions in the bulk fluid are dominated by forced convection, with rapid fluid acceleration occurring in the converging region of the channel and deceleration in the diverging region (Figs. 6(a) and (b)). The influence of assisting thermal buoyancy adjacent to the liquidus front again becomes significant as the flow decelerates near the chill section exit. Also, due to the adverse pressure gradient, boundary layer growth on the wall of the adiabatic exit region is pronounced. Flow reversal, while weak, occurs near the channel midplane (Fig. 6(b)) and results from the inability of the imposed flow to feed the strong thermally induced flow.

Figures 7–9 illustrate velocity, streamline, isotherm and liquid isocomposition distributions for Case 2 ($Re = 800$, $T_0 = 298$ K, $T_c = 233$ K, $f_{l,0}^{H_2O} = 0.72$) at selected times. Except for the Reynolds number, conditions are identical to those of Figs. 3–6.

Figure 7 illustrates conditions at $t = 120$ s and can be contrasted with Fig. 3. As with results for $Re = 200$, Fig. 7(a) reveals that solidification is initially characterized by rapid propagation of the liquidus front into the bulk fluid. While solidification again occurs both upstream and downstream of the chill section, the upstream effect is less pronounced due to the increased strength of the forced flow. For $Re = 800$, flow in the bulk fluid adjacent to the liquidus front inhibits the penetration of chilled, water-enriched interdendritic fluids across the permeable liquidus front. Hence, solutally driven upflows in the adiabatic entry region and the clockwise recirculation cell in the bulk fluid, which occurred for $Re = 200$ (Fig. 3), are not observed in Figs. 7(a) and (b). The absence of temperature and concentration gradients (Figs. 7(c) and (d)) upstream of the chill region confirms the strong influence which the imposed flow has on suppressing penetration of interdendritic fluid into the bulk fluid.

Within the mushy region, solutally driven flows of lighter, water-rich interdendritic fluid establish a recirculation pattern (Fig. 7(b)) in which upflow occurs near the solidus and downflow just inside the liquidus. Upflows nearest the solidus have the largest concentration of water and are able to ascend further than flows established closer to the liquidus. The ultimate path of the interdendritic fluid, as it ascends under the influence of positive solutal buoyancy forces, is strongly influenced by the strength of the imposed forced flow. For $Re = 200$ (Fig. 3(b)), shear forces induced at the permeable liquidus front are weak and interdendritic fluids are able to cross the front at the top of the mushy region. In contrast, for $Re = 800$ (Fig. 7(b)), shear forces induced by the imposed flow at and within the liquidus front deflect the ascending mushy region flow, thereby inhibiting penetration of the bulk liquid and inducing the observed mushy region recirculation. Irregularities in the liquidus front for $Re = 200$ (Fig. 3(a)), which were attributed to the water enrichment of bulk fluids upstream of the chill section and the corresponding liquidus temperature depression, are not observed in Fig. 7(a) for $Re = 800$.

The foregoing results, as well as those of a previous study for static solidification [5], confirm the significant influence of advection, whether naturally or externally induced, on redistribution of species in binary phase change processes. As for the strong thermally induced recirculation in the bulk fluid of static castings [5], the externally imposed forced flow of this study inhibits the penetration of solute-enriched interdendritic fluids into the melt and, hence, significantly influences subsequent phase change behavior.

Flow conditions in the bulk fluid for $Re = 800$ (Figs. 7(a) and (b)) differ significantly from those observed for $Re = 200$ (Figs. 3(a) and (b)). Due to the strength of the imposed flow, the influence of assisting thermal buoyancy on motion adjacent to the liquidus front is not discernible in the velocity field of Fig. 7(a). Moreover, the channeling of bulk fluids to feed thermally induced flows for small Re (Fig. 3(b)) is not observed in the streamline plots of Fig. 7(b).

Except for growth of the solid and mushy regions, conditions in Fig. 8 for $t = 240$ s ($t^* = 1.10 \times 10^{-3}$) are similar to those for $t = 120$ s (Fig. 7). Bulk fluid motion continues to inhibit penetration of interdendritic fluid across the liquidus front, confining the interdendritic flow to recirculation in the mushy region. Temperature and liquid composition gradients (Figs. 8(c) and (d)) are negligible in the bulk fluid,

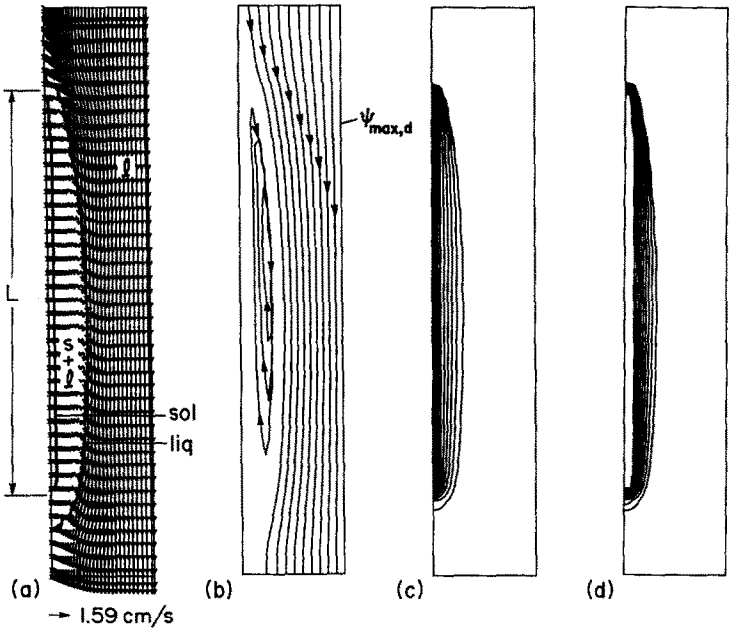

FIG. 7. Solidification behavior at $t = 120$ s ($t^* = 5.51 \times 10^{-4}$) for Case 2: (a) velocity vectors; (b) streamlines ($\psi_{max,d} = 2.60 \times 10^{-1}$, $|\psi_{max,r}| = 7.02 \times 10^{-4}$); (c) isotherms; (d) liquid isocomposition lines.

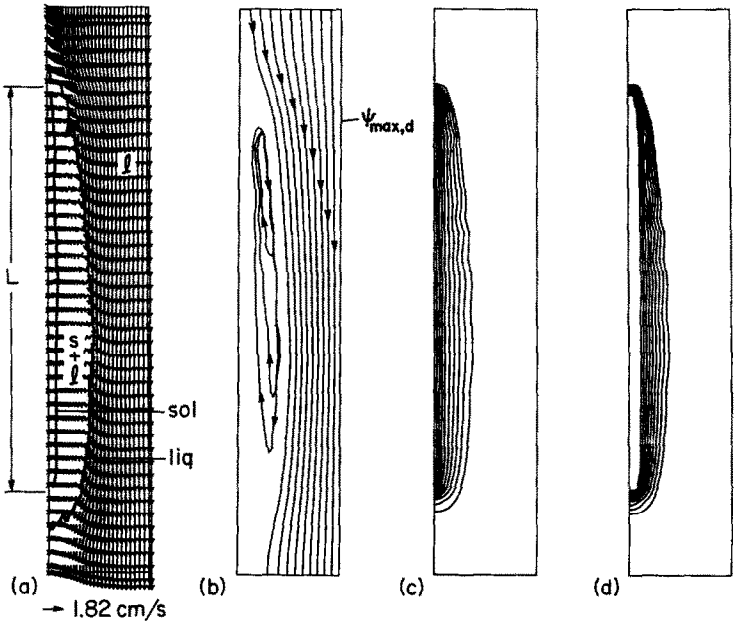

FIG. 8. Solidification behavior at $t = 240$ s ($t^* = 1.10 \times 10^{-3}$) for Case 2: (a) velocity vectors; (b) streamlines ($\psi_{max,d} = 2.60 \times 10^{-1}$, $|\psi_{max,r}| = 5.98 \times 10^{-4}$); (c) isotherms; (d) liquid isocomposition lines.

where motion is again dominated by the externally imposed flow.

During subsequent solidification at $t = 960$ s (Fig. 9(a)), liquidus temperature depression which accompanies water enrichment of the mushy region results in the formation of liquid pockets in this region. While confined liquid pockets were also predicted for $Re = 200$, the pockets of Fig. 9(a) are more sparsely distributed and do not form the elongated channels shown in Fig. 6(a). Also, the relatively smooth liquidus front near the chill section entrance for $Re = 800$ (Fig. 9(a)) contrasts sharply with the irregular liquidus front morphology of Fig. 6(a) for $Re = 200$.

Irregularities observed in the liquid isocomposition lines (Fig. 9(d)) correspond to locations of the mushy region liquid pockets. While interdendritic fluids remain confined to the mushy region, secondary recirculation cells were predicted (Fig. 9(b)) and are attributed to the influence of the pockets on flow in the mushy region.

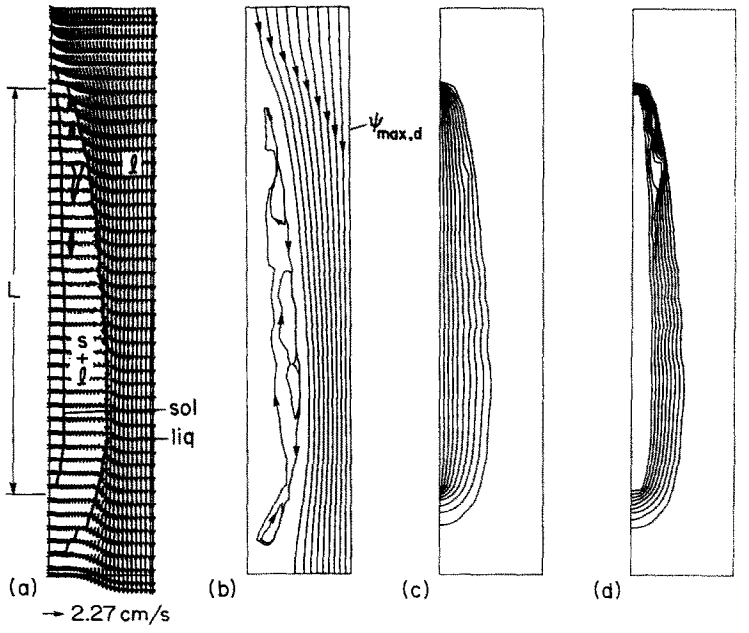

FIG. 9. Solidification behavior at $t = 960$ s ($t^* = 4.41 \times 10^{-3}$) for Case 2: (a) velocity vectors; (b) streamlines ($\psi_{max,d} = 2.60 \times 10^{-1}$, $|\psi_{max,r}| = 2.27 \times 10^{-4}$); (c) isotherms; (d) liquid isocomposition lines.

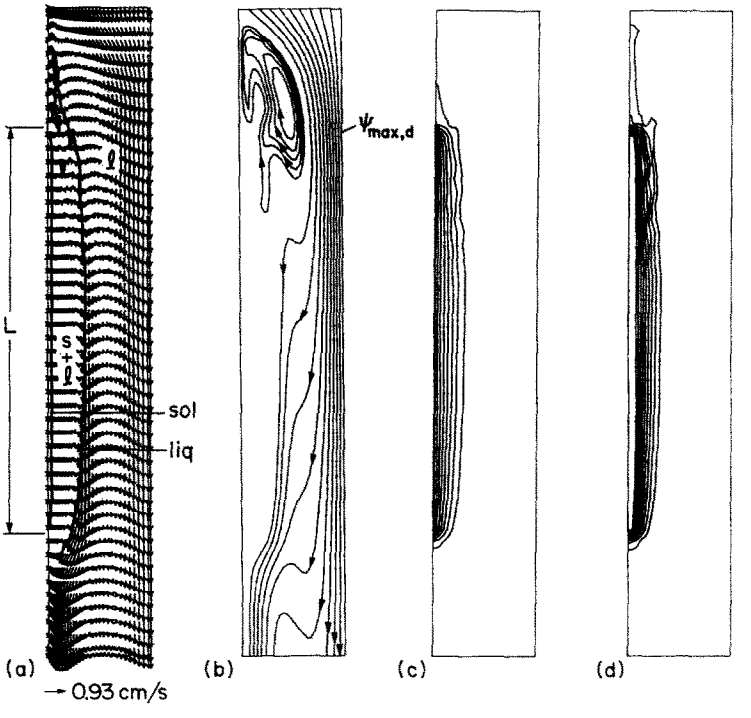

FIG. 10. Solidification behavior at $t = 120$ s ($t^* = 5.51 \times 10^{-4}$) for Case 3: (a) velocity vectors; (b) streamlines ($\psi_{max,d} = 6.50 \times 10^{-2}$, $|\psi_{max,r}| = 7.42 \times 10^{-3}$); (c) isotherms; (d) liquid isocomposition lines.

Figures 10–12 illustrate solidification behavior at representative times for Case 3 ($Re = 200$, $T_0 = 298$ K, $T_c = 243$ K, $f_{1,0}^{H_2O} = 0.72$). The influence of chill wall temperature T_c on solidification can be inferred by contrasting the results with those of Figs. 3–6 for $T_c = 233$ K.

Conditions in both the mushy and bulk fluid regions of Figs. 10–12 closely resemble those of Figs. 3–6. Hence, with minor exceptions, the trends of Figs. 10–12 ($T_c = 243$ K) are attributable to the same mechanisms used to describe the results of Figs. 3–6 ($T_c = 233$ K). The most noteworthy influence of increasing chill wall temperature is the reduction in growth of the solid phase. While the transient liquidus

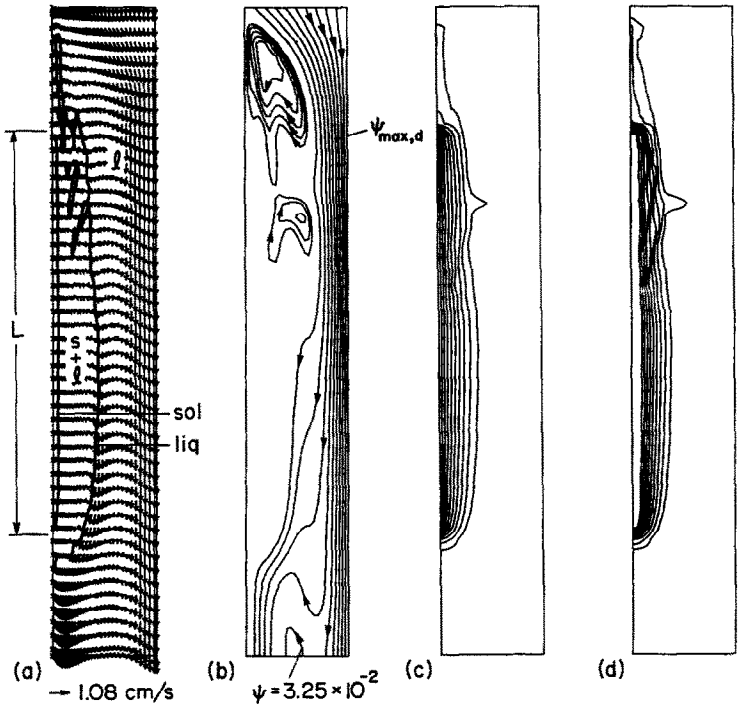

FIG. 11. Solidification behavior at $t = 240$ s ($t^* = 1.10 \times 10^{-3}$) for Case 3: (a) velocity vectors; (b) streamlines ($\psi_{max,d} = 6.50 \times 10^{-2}$, $|\psi_{max,r}| = 6.18 \times 10^{-3}$); (c) isotherms; (d) liquid isocomposition lines.

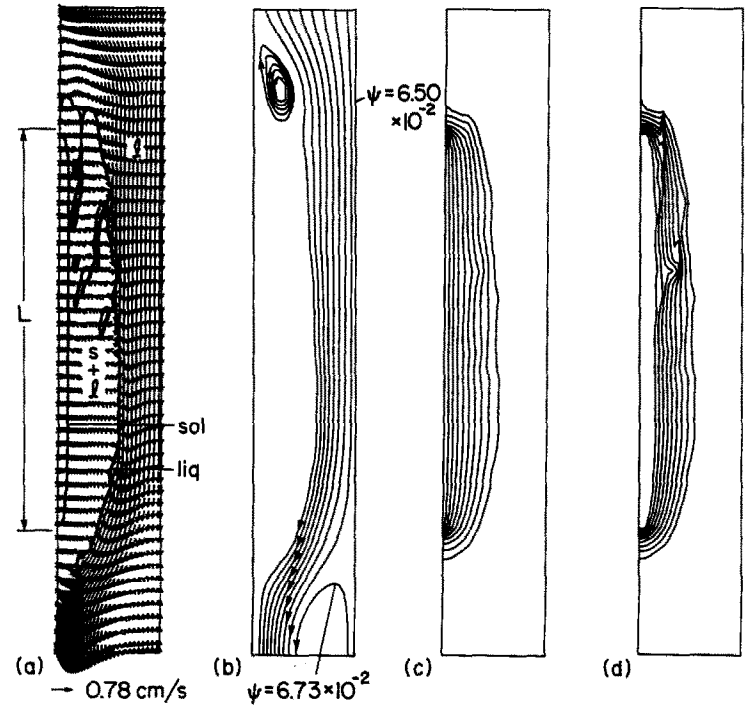

FIG. 12. Solidification behavior at $t = 960$ s ($t^* = 4.41 \times 10^{-3}$) for Case 3: (a) velocity vectors; (b) streamlines ($\psi_{max,d} = 7.47 \times 10^{-2}$, $|\psi_{max,r}| = 5.11 \times 10^{-3}$); (c) isotherms; (d) liquid isocomposition lines.

front locations of Figs. 3–6 are slightly larger than those of Figs. 10–12, growth of the pure solid region decreases considerably with increasing T_c. Previous experimental observations [20] have suggested that, with a reduction in solidification rate, the flow of interdendritic fluids, and hence solute redistribution, is enhanced. This observation is confirmed by Fig. 11(b), which reveals penetration of interdendritic fluids

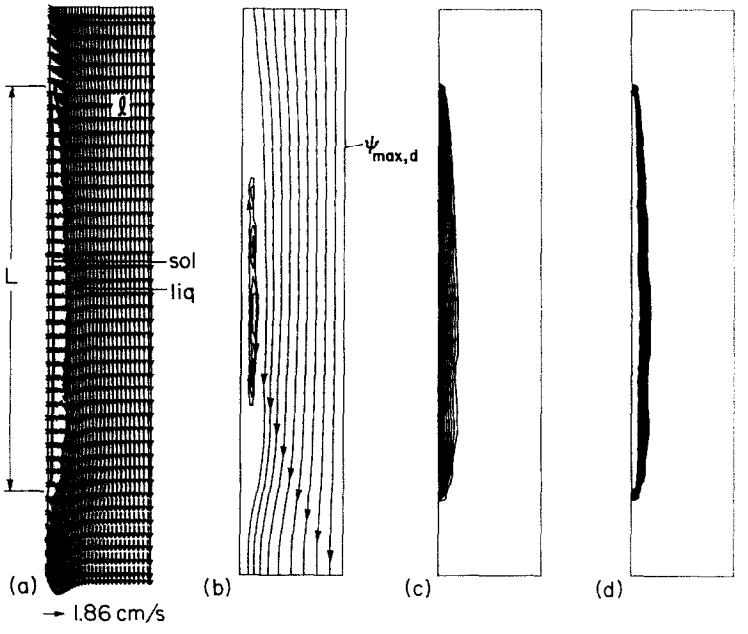

FIG. 13. Solidification behavior at $t = 120$ s ($t^* = 5.51 \times 10^{-4}$) for Case 4: (a) velocity vectors; (b) streamlines ($\psi_{max,d} = 2.60 \times 10^{-1}$, $|\psi_{max,r}| = 8.03 \times 10^{-5}$); (c) isotherms; (d) liquid isocomposition lines.

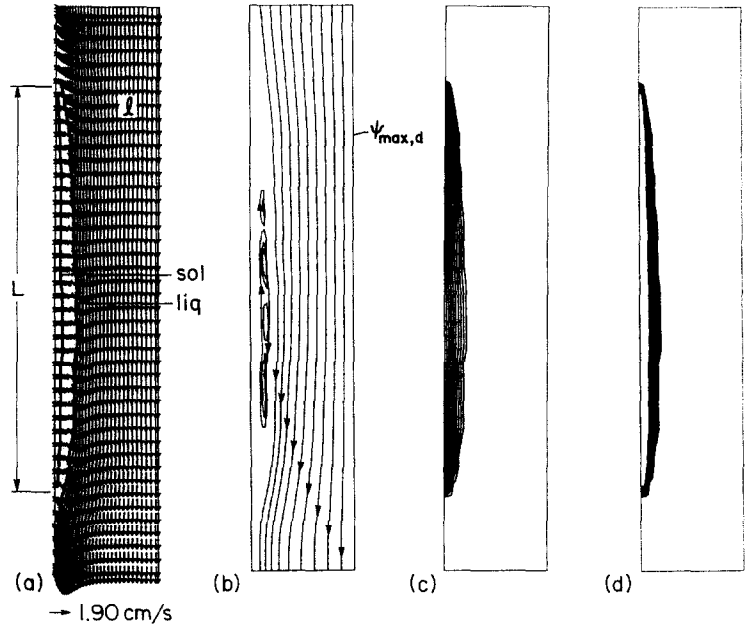

FIG. 14. Solidification behavior at $t = 480$ s ($t^* = 2.20 \times 10^{-3}$) for Case 4: (a) velocity vectors; (b) streamlines ($\psi_{max,d} = 2.60 \times 10^{-1}$, $|\psi_{max,r}| = 3.27 \times 10^{-5}$); (c) isotherms; (d) liquid isocomposition lines.

into the central, as well as the top, region of the bulk fluid. Penetration occurs through discrete flow channels which extend from the mushy region to the liquidus front (Fig. 11(a)). Irregularities in the isotherm and liquid isocomposition lines in the bulk fluid adjacent to the liquidus front (Figs. 11(c) and (d)) correspond to intersection of the mushy region flow channels with the fluid core and are consistent with outflows of chilled and water-enriched interdendritic fluids. Such penetration was not observed for conditions corresponding to lower chill wall temperatures and larger growth rates (Figs. 3–6). As solidification proceeds and conditions approach a steady state (Fig. 12), the solutally driven recirculation in the entrance region weakens and penetration of interdendritic fluids through discrete flow channels is no longer evident.

Figures 13 and 14 illustrate solidification behavior corresponding to selected times for Case 4 ($Re = 800$, $T_0 = 298$ K, $T_c = 233$ K, $f_{1.0}^{H_2O} = 0.73$). The influence of entry composition ($f_{1.0}^{H_2O}$) can be inferred by con-

trasting these results with those of Figs. 7–9 for $f_{1,0}^{H_2O} = 0.72$. The comparison reveals an extremely strong dependence of solidification on entry composition. Most noteworthy is the dramatic decline in solidification rates which accompany a 1% increase in entry water composition. The primary cause of this decline is the corresponding depression in the liquidus temperature. Due to the extremely large liquidus slope for the NH_4Cl–H_2O system (Fig. 2), a change in $f_{1,0}^{H_2O}$ from 0.72 to 0.73 results in a 4.7°C depression in liquidus temperature. The decrease in T_{liq} which accompanies an increase in $f_{1,0}^{H_2O}$ increases the temperature difference $(T_0 - T_{liq})$ and hence increases energy transport from the bulk fluid to the mushy region. It is this enhancement of interfacial energy transport which is responsible for the decline in solidification rates.

With increasing temperature difference $(T_0 - T_{liq})$, the influence of assisting (downward) thermal buoyancy on bulk fluid motion also increases. While flow conditions in the bulk fluid for $f_{1,0}^{H_2O} = 0.72$ (Figs. 7(a)–9(a)) were dominated by forced convection, mixed convection behavior is discernible near the liquidus front for $f_{1,0}^{H_2O} = 0.73$ (Figs. 13(a) and 14(a)). In particular, the increased influence of thermal buoyancy relative to the imposed flow leads to fluid acceleration and velocity boundary layer development on the liquidus front.

Interdendritic flows are confined to recirculation within the mushy region (Figs. 13(b) and 14(b)) and, due to the relatively thin mushy region and small permeabilities, are significantly weaker than those observed for $f_{1,0}^{H_2O} = 0.72$ (Figs. 7(b)–9(b)). The formation of liquid pockets is not predicted and, as shown in Figs. 13(c), (d) and 14(c), (d), the bulk fluid remains free of significant temperature and liquid composition gradients. In contrast, temperature and liquid composition gradients within the solid and mushy regions are large due to the relatively small thickness of these regions.

4. CONCLUSIONS

The displacement of segregated liquids within the multiphase region of solidifying multiconstituent systems is generally considered to be the most important cause of undesirable macroscopic species redistribution. In addition to being influenced by the complex microscopic structure of the multiphase region, this redistribution is governed by the interaction of multiphase region fluids with adjoining bulk fluids. For statically cast binary systems, in which flows are driven entirely by buoyancy, it has been shown [5] that the extent of penetration of multiphase region fluids across the permeable liquidus interface is governed by the relative strengths of solutally driven mushy region flows and thermally driven flows in the bulk liquid. Similarly, for the mixed convection conditions of this study, the advection of mushy region fluids across the liquidus is governed by the relative strengths of the solutally driven mushy region flow and externally imposed forced flow. Strong externally induced flows were shown to inhibit the penetration of solute rich mushy region fluids across the permeable liquidus, causing penetration to decrease with increasing Reynolds number. Penetration also decreased with decreasing chill wall temperature, which had the effect of enhancing solidification rates and reducing mushy region advection. Due to the extreme sensitivity of liquidus temperature to liquid species composition, solidification was found to depend strongly on the inlet composition.

Acknowledgements—Support of this work by the U.S. Department of Energy under Award Number DE-FG02-87ER13759 is gratefully acknowledged. The research was conducted at Purdue University while one author (WDB) was on a supported technical leave of absence from the Aluminum Company of America.

REFERENCES

1. R. Mehrabian, M. Keane and M. C. Flemings, Interdendritic fluid flow and macrosegregation: influence of gravity, *Metall. Trans.* **1,** 1209–1220 (1970).
2. T. Fujii, D. R. Poirier and M. C. Flemings, Macrosegregation in a multicomponent low alloy steel, *Metall. Trans. B* **10,** 331–339 (1979).
3. S. D. Ridder, S. Kou and R. Mehrabian, Effect of flow on macrosegregation in axisymmetric ingots, *Metall. Trans. B* **12B,** 435–447 (1981).
4. J. Szekely and A. S. Jassal, An experimental and analytical study of the solidification of a binary dendritic system, *Metall. Trans. B* **9B,** 389–398 (1978).
5. W. D. Bennon and F. P. Incropera, A continuum model for momentum, heat and species transport in binary solid–liquid phase change systems—II. Application to solidification in a rectangular cavity, *Int. J. Heat Mass Transfer* **30,** 2171–2187 (1987).
6. W. D. Bennon and F. P. Incropera, The evolution of macrosegregation in statically cast binary ingots, *Metall. Trans. B* **18B,** 611–619 (1987).
7. J. Szekely and V. Stanek, On heat transfer and liquid mixing in the continuous casting of steel, *Metall. Trans.* **1,** 119–126 (1970).
8. S. Kou, D. R. Poirier and M. C. Flemings, Macrosegregation in rotated remelted ingots, *Metall. Trans. B* **9B,** 711–719 (1978).
9. M. Choudary and J. Szekely, The modeling of pool profiles, temperature profiles and velocity fields in ESR systems, *Metall. Trans. B* **11B,** 439–453 (1980).
10. F. B. Cheung and M. Epstein, Solidification and melting in fluid flow. In *Advances in Transport Processes* (Edited by A. S. Mujumdar and R. A. Mashelkar), Vol. 3, pp. 35–117. Wiley, New Delhi (1984).
11. W. D. Bennon and F. P. Incropera, A continuum model for momentum, heat and species transport in binary solid–liquid phase change systems—I. Model formulation, *Int. J. Heat Mass Transfer* **30,** 2161–2169 (1987).
12. S. Asai and I. Muchi, Theoretical analysis and model experiments on the formation mechanism of channel-type segregation, *Trans. ISIJ* **18,** 90–98 (1978).
13. S. V. Patankar, *Numerical Heat Transfer and Fluid Flow*. Hemisphere, Washington, DC (1980).
14. W. D. Bennon and F. P. Incropera, Numerical analysis of binary solid–liquid phase change using a continuum model, *Numer. Heat Transfer* (1988), in press.
15. J. R. Bodia, The finite difference analysis of confined

viscous flows, Ph.D. Thesis, Carnegie Institute of Technology, Pittsburgh, Pennsylvania (1959).
16. *International Critical Tables of Numerical Data, Physics, Chemistry, and Technology*, Vols 3 and 4 (1928).
17. K. A. Jackson, J. D. Hunt, D. R. Uhlmann and T. P. Seward, III, On the origin of the equiaxed zone in castings, *Trans. Metall. Soc. A.I.M.E.* **236,** 149–158 (1966).
18. R. J. McDonald and J. D. Hunt, Fluid motion through the partially solid regions of a casting and its importance in understanding A type segregation, *Trans. Metall. Soc. A.I.M.E.* **245,** 1993–1997 (1969).
19. S. M. Copley, A. F. Giamei, S. M. Johnson and M. F. Hornbecker, The origins of freckles in unidirectionally solidified castings, *Trans. Metall. Soc. A.I.M.E.* **1,** 2193–2204 (1970).
20. S. Kou, D. R. Poirier and M. C. Flemings, Macrosegregation in electroslag remelted ingots, *AIME Electric Furnace Conference Proceedings*, pp. 221–228 (1977).

SIMULATION NUMERIQUE DE LA SOLIDIFICATION BINAIRE DANS UN CANAL VERTICAL AVEC CONVECTION MIXTE THERMIQUE ET SOLUTALE

Résumé—Un modèle continu est utilisé pour étudier la solidification d'une solution aqueuse de chlorure d'ammonium en présence d'un écoulement forcé. Des calculs déterminent l'effet du débit, de la température de paroi froide et de la composition du liquide à l'entrée, sur les transferts de quantité de mouvement, d'énergie et d'espèces dans la multiphase et le liquide. Des petits débits-masse et des faibles vitesses de solidification augmentent l'écoulement libre des fluides glacés et interdendritiques enrichis en eau, à travers le front perméable de liquidus et par suite accroît la redistribution des espèces.

NUMERISCHE SIMULATION DES ERSTARRUNGSVORGANGES EINES ZWEISTOFFGEMISCHES IN EINEM VERTIKALEN KANAL BEI THERMISCHER UND KONZENTRATIONSBEDINGTER MISCHKONVEKTION

Zusammenfassung—Zur Untersuchung des Erstarrungsvorganges einer wässrigen Ammonium-Chlorid-Lösung bei erzwungener Strömung wird ein Kontinuums-Modell benutzt. Damit wurde der Einfluß des Massenstroms, der Kühlflächentemperatur und der Zusammensetzung der eintretenden Flüssigkeit auf den Impuls-, Energie- und Stofftransport sowohl im mehrphasigen Randbereich als auch im flüssigen Kern berechnet. Es zeigt sich, daß geringe Massenströme und Erstarrungsgeschwindigkeiten die freie Strömung von abkühlenden bzw. mit Wasser angereicherten interdentritischen Fluiden durch die permeable Liquidus-Front steigern. Dadurch nimmt die Rückverteilung der Komponenten zu.

ЧИСЛЕННОЕ МОДЕЛИРОВАНИЕ ЗАТВЕРДЕВАНИЯ БИНАРНОЙ ЖИДКОСТИ В ВЕРТИКАЛЬНОМ КАНАЛЕ СО СМЕШАННОЙ ТЕПЛОВОЙ И КОНЦЕНТРАЦИОННОЙ КОНВЕКЦИЕЙ

Аннотация—Используется модель сплошной среды для исследования затвердевания водного раствора хлористого аммония при вынужденном течении. Расчеты выполнены с целью определения влияния расхода, температуры закалки и состава жидкости на входе на количество движения, перенос энергии и компонентов внутри как многофазной, так и сплошной сред. Показано, что при небольших значениях массового расхода и скорости затвердевания свободное течение охлажденной и водонасыщенной междендритной жидкости поперек проницаемого фронтаусиливается, а тем самым усиливается и перераспределение компонентов.